

Realization of 2D Crystalline Metal Nitrides via Selective Atomic Substitution

Jun Cao^{1†}, Tianshu Li^{2†}, Hongze Gao², Yuxuan Lin⁴, Xingzhi Wang¹, Haozhe Wang⁴, Tomás Palacios⁴, Xi Ling^{1,2,3*}

1. Department of Chemistry, Boston University, 590 Commonwealth Avenue, Boston, MA 02215, USA.

2. Division of Materials Science and Engineering, Boston University, 15 St. Marys Street, Boston, MA 02215, USA.

3. The Photonics Center, Boston University, 8 St. Marys Street, Boston, MA 02215, USA.

4. Department of Electrical Engineering and Computer Science, Massachusetts Institute of Technology, Cambridge, MA 02139, USA.

[†]These authors contributed equally to this work.

*Corresponding author. Email: xiling@bu.edu (X.L.)

Abstract

Two-dimensional (2D) transition metal nitrides (TMNs) are new members in the 2D materials family with a wide range of applications. Particularly, highly crystalline and large area thin films of TMNs are potentially promising for applications in electronic and optoelectronic devices; however, the synthesis of such TMNs has not yet been achieved. Here, we report the synthesis of few-nanometer thin Mo_5N_6 crystals with large area and high quality via *in situ* chemical conversion of layered MoS_2 crystals. The structure and quality of the ultrathin Mo_5N_6 crystal are confirmed using transmission electron microscopy, Raman spectroscopy and X-ray photoelectron spectroscopy. The large lateral dimensions of Mo_5N_6 crystals are inherited from the MoS_2 crystals that are used for the conversion. Atomic force microscopy characterization reveals the thickness of Mo_5N_6 crystals is reduced to about 1/3 of the MoS_2 crystal. Electrical measurements show the obtained Mo_5N_6 samples are metallic with high electrical conductivity ($\sim 100 \text{ } \Omega \text{ sq}^{-1}$), which is comparable to graphene. The versatility of this general approach is demonstrated by expanding the method to synthesize W_5N_6 and TiN . Our strategy offers a new direction for preparing 2D TMNs with desirable characteristics, opening a door for studying fundamental physics and facilitating the development of next generation electronics.

Introduction

Transition metal nitrides (TMNs) are well-known for their high melting points, hardness and chemical inertness (1, 2). The successful preparation of two-dimensional (2D) MXenes through selectively etching the “A” layer of bulk MAX phase triggered the study of 2D metal carbides and nitrides since 2011 (3–6). Although a variety of carbide MXenes have been synthesized using this method, the synthesis of nitrides MXenes is limited to Ti_4N_3 and Ti_2N (7, 8), due to the low availability of bulk MAXs for corresponding 2D metal nitrides. Urbankowski et al. further reported the synthesis of multilayer molybdenum and vanadium nitrides by ammoniation of carbide MXenes synthesized using the selective etching method (9). Currently, as-synthesized 2D TMNs are either in solution phase or in powder form, and the lateral sizes of the flakes are usually small (< 10 micrometers) (10–15). In addition, samples prepared by selective etching suffer from defects generated during the etching process and large thickness distributions (16, 17). These types of 2D TMNs are not suitable for high performance electronic and optoelectronic device applications which often require 2D crystals with decent area (>10 micrometers of lateral size), quality, and deposition on solid state substrates (18, 19). Conventional 2D materials such as graphene and transition metal dichalcogenides (TMDs) produced using chemical vapor deposition (CVD) have made significant progress in advancing the development of electronic devices (20–22). In contrast to many conventional 2D materials with strong in-plane covalent bonds and weak out-of-plane van der Waals interactions between the layers, the van der Waals gap is missing in bulk TMN crystals. Instead, covalent bonding extends in three-dimensional (3D) frameworks of TMNs. Thus, conventional methods such as top-down mechanical exfoliation and bottom-up CVD, which take advantage of the weak interlayer van der Waals interaction and self-limited in-plane growth, are ineffective for the synthesis of large-area and ultrathin 2D TMNs. Therefore, developing effective

routes to synthesize 2D TMN crystals with desired morphology and quality is essential to realize the potential for applications toward electronic devices.

Using nitriding reaction of metal oxides, TMDs and transition metal carbides (TMCs) to synthesize bulk TMNs is an established process (23–28). Recently, transformation of 2D MoS₂ and TMCs to 2D TMNs while retaining crystal structure was demonstrated in an ammonia atmosphere (9, 27). This transformation method is promising for large-area synthesis of 2D TMNs, considering the well-established preparation methods TMDs thin films with controlled thickness and various lateral dimensions ranging from micrometer size to wafer scale (22, 29, 30). However, the precursors used in the reported work for the transformation are either multilayered carbide MXenes or powder TMDs (9, 27). The obtained 2D TMNs are still marred by large thickness distributions, defective structures and small lateral sizes passed on from the precursors. Furthermore, an atomic level investigation of the transformation, which is the key to evaluate the potential of the strategy for producing high-quality and large-area 2D TMN crystals, is lacking.

Here, beginning with a precursor layer of MoS₂, an *in situ* transformation from MoS₂ to ultrathin Mo₅N₆ is achieved. Optical and scanning electron microscopic (SEM) images show that the geometry and morphology of the crystals are retained during the transformation. The obtained Mo₅N₆ exhibits high crystallinity over the entire area. *In situ* transformations of various MoS₂ flakes down to 4 layers for Mo₅N₆ flakes with different thicknesses are achieved. Atomic force microscopic (AFM) analysis shows that the thickness of most of MoS₂ flakes is reduced by about 2/3 after the transformation. Electrical measurements show the high conductivity of metallic Mo₅N₆ samples. We further demonstrate that such strategy can be applied to other TMDs such as WS₂ and TiS₂ for preparing their corresponding TMNs. This work opens a new direction for preparing 2D TMNs with desired quality that are previously inaccessible.

Results

Figure 1 shows a schematic illustration of the typical reaction process. The conversion was performed in a horizontal tube furnace (See Materials and Methods for details of synthesis). MoS₂ flakes with different thicknesses were prepared using mechanical exfoliation and transferred onto a SiO₂/Si substrate, which was then placed at the center of the furnace. A crucible filled with urea was placed in the upstream zone of the furnace, serving as the ammonia gas source which was released from the thermolysis of urea at 200 °C (31, 32). 100 sccm Ar gas was used as carrier gas. The temperature in the center of the furnace was set at 750~800 °C for the chemical reaction between gaseous ammonia and MoS₂ flakes (23, 27). Apart from Mo₅N₆ which was the solid product, the other two side products, H₂S and N₂ were in gaseous phase and carried away by the Ar gas (23, 27), leaving clean Mo₅N₆ products with minimum contaminants.

Figure 2 (A and B) shows optical images of a 12.9 nm MoS₂ flake before and after the reaction. The optical contrast of the flake changed dramatically after the reaction, but the morphology and shape of flakes are retained. Conversion results of more MoS₂ flakes with different thicknesses ranging from ~3 nm to tens of nanometers are shown in fig. S1. All MoS₂ flakes displayed significant changes of optical contrast after conversion. Absorption spectra (fig. S2) of the flake before (MoS₂) and after (Mo₅N₆) the conversion suggest that such change originated from the distinct optical properties, consistent with the distinct electronic band structures of the two materials (15, 33). More evidence supporting the successful conversion of MoS₂ to Mo₅N₆ is reported in the later section. Atomic force microscopy (AFM) images show the atomically smooth surface of the flakes after conversion (fig. S3), suggesting a mild conversion process during which the reaction is confined within the original MoS₂ flakes. We further measured the Raman and photoluminescence (PL) spectra of the flake before and after the chemical transformation. As

shown in Fig. 2C, pronounced A_{1g} and E_{2g}^1 modes at ~ 384 and ~ 407 cm^{-1} (34, 35) were observed from MoS_2 flakes before the transformation. Both modes vanished completely after the reaction and new Raman peaks at ~ 215 and 710 cm^{-1} appeared, indicating the transformation of the crystal domain. Similarly, PL from MoS_2 disappeared after the conversion (Fig. 2D) (33, 36), matching well with the semiconducting and metallic property of MoS_2 and Mo_5N_6 (15, 33). In addition, Raman mapping results (Fig. 2, E and F) indicated the entire flake was converted from MoS_2 to Mo_5N_6 , where no Raman signals from MoS_2 was observed on the converted flake globally. Corresponding PL mapping results are shown in fig. S4.

To determine the phase and crystal structure of the flake, we performed transmission electron microscopy (TEM) characterization on an as-prepared sample. The low magnification TEM image in Fig. 3A shows the smooth surface of the flake where the small variations of the contrast are due to the wrinkles generated during the transfer process. The selected-area electron diffraction (SAED) pattern in Fig. 3B (see also fig. S5) indicates the high crystallinity of the sample. Same SAED pattern was observed when measuring on different regions of the flake. The hexagonal diffraction pattern is consistent with the crystal structure of the Mo_5N_6 (15). The experimental and simulated SAED patterns (fig. S5) of Mo_5N_6 match well with each other. High-angle annular dark-field (HAADF) scanning transmission electron microscope (STEM) image is shown in Fig. 3C, where Mo atoms and atomic lattice are clearly seen and no obvious defect is found in the sample. N atoms are invisible under our STEM condition due to the small atomic number compared to Mo atoms. Additionally, the distance of 0.239 nm between the lattice planes is consistent with the d-spacing of (110) planes in Mo_5N_6 crystal, which matches with the SAED pattern. We also noticed that the obtained Mo_5N_6 crystal had an enhanced stability under 200 keV electron beam compared to MoS_2 flakes (37, 38), where Mo_5N_6 flakes on TEM grid remained stable without noticeable change after

being exposed under electron beam for 30 minutes (fig. S6), providing an additional advantage for future applications in electronic devices. STEM imaging and energy-dispersive spectroscopy (EDS) mapping were performed (see fig. S5) on a thick Mo_5N_6 flake which provides better signal-to-noise ratio of EDS signal. Dark field STEM image shows the inhomogeneous contrast of the thick Mo_5N_6 flake (fig. S5), which is probably due to strong local strain during the conversion process. EDS mapping of N K peak and Mo L peak (fig. S5) shows uniform distribution of Mo and N elements in the flake. The TEM characterization confirmed that the highly crystalline Mo_5N_6 flake was successfully obtained through the chemical transformation.

The chemical composition and oxidation states of the elements in sample Mo_5N_6 were characterized using X-ray photoelectron spectroscopy (XPS) and EDS analyses. Figure 3D shows the XPS wide scan survey spectrum of the sample, where significant Mo and N signals are observed and no signal from S appeared, indicating complete conversion of MoS_2 to Mo_5N_6 . Other elements such as O, Si and C are from the SiO_2/Si substrate and the chamber environment. Similar results were obtained from EDS characterization (fig. S7). High-resolution XPS spectra deconvolution for the N 1s, Mo 3p and Mo 3d regions are shown in Fig. 3 (E and F). The N 1s peak at 397.9 eV and Mo 3p $_{3/2}$ at 395.3 eV (Fig. 3E) suggest that chemical bond formed between Mo and N (15). In the Mo 3d region (Fig. 3F), the peaks at 233.0 eV and 229.8 eV were assigned to the binding energies of Mo 3d $_{3/2}$ and Mo 3d $_{5/2}$, respectively (39), with a spin-orbit splitting of 3.2 eV. This characteristic doublet of core-level Mo 3d $_{5/2}$ and 3d $_{3/2}$ indicates that Mo (+4) oxidation state dominates in Mo_5N_6 (25). Nevertheless, the binding energy of 229.8 eV is slightly smaller than reported value at 230.0 eV for Mo (+4) oxidation state (15), suggesting the co-existence of Mo (+3) oxidation state in the sample. No peaks corresponding to higher oxidation

states of Mo from MoO_x were observed in the Mo 3d region (40), ruling out the possibility of the formation of MoO_x.

To address the mechanism by which the lattice changed during the atomic substitution from MoS₂ to Mo₅N₆, we investigated thickness changes of flakes before and after chemical conversion. The crystal structure models of MoS₂ and Mo₅N₆ (Fig. 4, A and B) predict that the van der Waals gap between MoS₂ layers will disappear during the transformation to Mo₅N₆ crystals, leading to the reducing of the thickness from MoS₂ to Mo₅N₆. The distance between two Mo layers in MoS₂ is 7.66 Å (41), while it is 2.77 Å in Mo₅N₆ (42), therefore the thickness of the flake can be predicted to decrease to 36% when transforming from MoS₂ to Mo₅N₆. To test this hypothesis, we performed AFM to extract the thickness of flakes. As expected we observed that the thickness was reduced post chemical transformation. Figure 4C and D show typical AFM images of MoS₂ and corresponding Mo₅N₆ flake, where they have nearly the same morphology and both surfaces are smooth. However, the thickness of the flake decreased from 9.5 nm for MoS₂ to 3.5 nm for Mo₅N₆ (Fig. 4E), where Mo₅N₆/MoS₂ thickness ratio is 37%. Furthermore, we performed this comparison for ~30 flakes with MoS₂ thickness ranging from few nanometers to ~35 nm. Reduced sample thickness was observed for all flakes after conversion (Fig. 4F). The average Mo₅N₆/MoS₂ thickness ratio is 56% based on the slope of linear fitting curve, but for MoS₂ flakes with the thickness of 5 to 15 nm, the ratio is around 40%, matching well with the expected value. For thinner flakes, the ratio is larger, probably because the termination groups on the surface are non-negligible at this size range (3, 5) or the substrate roughness introduces a large uncertainty for the measurement. Figure S8 shows a 4-layer MoS₂ flake (3.4 nm) turned to a 2.1 nm Mo₅N₆ flake after conversion. Note that we found the morphology and quality of the flake remain well at such thin level. Based on the morphology retaining and thickness depression phenomena observed in our

experiments, we propose the following mechanism of the chemical transformation from MoS₂ to Mo₅N₆. When NH₃ gas diffuses into the van der Waals gaps of the MoS₂ flake, one N atom will replace two S atoms sandwiched by two adjacent Mo layers. When Mo-S bonds around a Mo atom are broken, six binding sites on the Mo atom will be released. Each N atom will then bond with six Mo atoms to form Mo₅N₆, where adjacent Mo layers are bridged by the N atoms, leading to the vanishing of the van der Waals gaps that originally exist in MoS₂. In this process, breaking Mo-S bonds and forming Mo-N bonds do not require large rearrangements of Mo atoms, even though small shift of positions of Mo atoms may be necessary to compensate the bond length difference between Mo-S and Mo-N. In fact, despite the layered structure of MoS₂ (point group: D_{6h}, space group: P6₃/mmc) (41) and non-layered nature of Mo₅N₆ (point group: C_{6h}, space group: P 6₃/m) (42), the Mo layers in these two materials are both in hexagonal pattern. This similarity in structure allows gentle transformation without structural collapse, leading to the morphology retaining of samples before and after chemical transformation.

To further investigate the transformation process, we performed the reaction under varying conditions. We found that excess amount of urea, which provided sufficient NH₃ gas in the chamber, was a key factor for the success because it ensured a reducing environment to prevent MoS₂ from oxidation (fig. S9). Additionally, the degree of conversion could be tuned by changing the reaction temperature and time. A complete conversion occurred within 5 minutes when the reaction temperature varied from 750 °C to 800 °C (fig. S9). However, at 700 °C, the conversion was only partially complete even after 60 minutes, where only the edge area was converted and no Mo₅N₆ was observed in the central region of the flake (fig. S10), indicating that the conversion started from the edge of the MoS₂ flake. Because of the partial conversion, we realized a lateral heterostructure between MoS₂ and Mo₅N₆ through a simple partial conversion. The successful

synthesis of such heterostructure offers a great platform for future study on the junction properties and applications. Moreover, the converted Mo_5N_6 showed excellent stability, where the crystal structure remained intact after 6 months and survived in acetone, DI water and 1 mol/L H_2SO_4 solution for at least 2 hours without noticeable changes from optical images and Raman spectra (fig. S11). This is advantageous to be compatible with future device fabrication process.

To examine the property of the converted Mo_5N_6 sample, we fabricated a back gate transport device on a 9.5 nm thick Mo_5N_6 flake (Fig. 5A and fig. S13). The gate-dependence of the transport current shows that the drain-source current (I_{ds}) remained constant as the gate voltage scanned from -20 V to 20 V and variations of I_{ds} was still negligible even when noise signal became visible, featuring metallic behavior of the as-synthesized Mo_5N_6 sample (Fig. 5B). We further performed the temperature-dependent transport measurement down to 77 K to investigate the electrical conductivity of the sample. Fig. 5C shows the output I - V characteristics through a 4-probe measurement where slope of the I - V curves increases very slowly as the temperature increases from 77 K to 240 K (Fig. 5C, inset). The sheet resistances of Mo_5N_6 at different temperatures were extracted from the slope of I - V curves and the dimension of the transport device (Fig. 5D), using the formula $R_s = R \times (W/L)$. R is the total electrical resistance of the device, and W and L are the effective width and length of the measurement area, which are measured as 3.4 and 6.1 μm from the optical image, respectively. Low sheet resistances of Mo_5N_6 ranging from 114.4 to 117.8 $\Omega \text{ sq}^{-1}$ were obtained under different temperatures, which is in the same order of magnitude of CVD graphene (43). The fact that the sheet resistance of Mo_5N_6 is not sensitive to the temperature change from 77 K and 240 K is consistent with the trend of transition metal nitrides reported in the literature (9).

We further applied this strategy to the conversion from WS₂ and TiS₂ to their corresponding nitrides (See Materials and Methods for details of the synthetic conditions). Figure 6 shows a typical conversion result on a 5.6 nm WS₂ and a ~100 nm TiS₂ flake. As shown in Fig. 6A-H, significant optical contrast change was observed from WS₂ and W₅N₆, as well as from TiS₂ to TiN. Similar to the case of MoS₂ to Mo₅N₆ conversion, the morphology of the flakes was retained. Raman characterization showed that the Raman signatures from WS₂ and TiS₂ disappeared completely (44, 45). Instead, new peaks that correspond to the phonon modes of W₅N₆ (e.g. ~258 cm⁻¹) and TiN (e.g. ~154 and 620 cm⁻¹) (46, 47) appeared (Fig. 6, I to J), indicating a successful chemical conversion. The Raman mapping results clearly show that the conversion is thorough and uniform. More optical and corresponding SEM images of W₅N₆ (fig. S12) and TiN (fig. S12) corroborate uniform surface of converted samples. Phase and crystallinity of W₅N₆ are characterized by HRTEM and EDS analyses (fig. S14) (48). Similar to Mo₅N₆, W₅N₆ and TiN also exhibit excellent stability against acetone, DI water and 1 mol/L H₂SO₄ for at least 2 hours (fig. S11).

Discussion

We demonstrate a versatile conversion strategy from layered TMDs to their corresponding ultrathin nitrides through atomic substitution from chalcogen to nitrogen. This method facilitates the production of 2D crystalline TMNs including Mo₅N₆, W₅N₆ and TiN, offering a pathway toward an important class of 2D materials that previously are inaccessible. The investigation of the *in situ* transformation from MoS₂ layers to 2D Mo₅N₆ crystals shows reduced thickness after conversion. 2D Mo₅N₆ crystal as thin as 2.1 nm is achieved by converting a 4-layer MoS₂. The electrical measurement shows that the converted Mo₅N₆ is metallic with high conductivity of about 100 Ω sq⁻¹. By controlling the reaction rate, we achieve a Mo₅N₆-MoS₂ lateral heterostructure,

demonstrating the advantage of our method in integrating 2D materials together for basic building blocks (e.g. metal-semiconductor junction) for future applications for electronic devices. More importantly, building on the success of the TMDs synthesis in the field (21, 22, 30), we anticipate the strategy we report here will lead to effective synthesis of large-area and high quality 2D TMNs that satisfy the needs for high performance electronic and optoelectronic devices.

MATERIALS AND METHODS

Conversion from TMDs to TMNs

MoS₂, WS₂ and TiS₂ with different thicknesses were prepared using mechanical exfoliation method from their bulk crystals (purchased from HQ Graphene) and transferred onto 300 nm SiO₂/Si substrates. Note that SiO₂/Si substrates were cleaned by sonication in water, acetone, and isopropanol solvents sequentially (each 10 minutes), followed by O₂ plasma cleaning before use. Chemical conversions were conducted in a horizontal tube furnace where Ar gas was introduced into the tube and the flow was controlled by a mass flow controller. Samples were placed in a 1-inch diameter quartz tube in the center of the furnace. Excess amount of urea (500 mg) was placed in an Al₂O₃ crucible located upstream of the furnace, serving as nitrogen source. After purging with Ar gas for 10 minutes, the tube was heated to 800 °C with a 30-min ramp. The conversion time for Mo₅N₆ and TiN is 1 hour, and it is 2 hours for W₅N₆. Throughout the conversion, 100 sccm Ar flow was used to maintain the inert atmosphere. When conversion was completed, the system was cooled down naturally.

Materials characterizations

As-prepared TMNs were characterized using Raman spectroscopy, AFM, TEM, STEM, SAED XPS and EDS. Raman and PL measurements were performed on a Renishaw inVia Raman

microscope equipped with a 532 nm laser line. All the spectra in comparison were taken using the same condition. The AFM topography was acquired on a Bruker Dimension system. TEM measurements were performed on a FEI Tecnai Osiris transmission electron microscope, operating at a 200 keV accelerating voltage. SAED were measured on a JEOL 2100 transmission electron microscope. The SAED simulation was performed through STEM_CELL software (49). Atomic resolution STEM and EDS mapping was performed on a JEOL ARM 200F scanning transmission electron microscope, operating at 200 keV. XPS measurements were performed under ultrahigh vacuum below 2×10^{-9} Torr using monochromatic Al K α radiation at 1486.7 eV on a Surface Science Instruments SSX100 spectrometer.

Fabrication and conductivity measurements

The electrical transport device was fabricated through laser writer lithography and thermal evaporation of 5 nm Cr and 45 nm Au. For lift-off, the sample was soaked in Remover PG at 60°C for 10 minutes to remove the photoresist and then washed in isopropanol and deionized water. Device characterization was performed using a semiconductor parameter analyzer (Keysight B1500A) and a Lakeshore cryogenic probe station with micromanipulation probes and liquid nitrogen cooling. All measurements were done in vacuum ($< 3 \times 10^{-6}$ Torr).

SUPPLEMENTARY MATERIALS

Fig. S1. Typical optical images of MoS₂ and Mo₅N₆ flakes with different thicknesses.

Fig. S2. Absorption spectra of MoS₂ and Mo₅N₆ samples on quartz substrate.

Fig. S3. AFM images of MoS₂ and Mo₅N₆ flakes in Figure (2).

Fig. S4. Maps of PL intensity at 673 nm of MoS₂ (A) and Mo₅N₆ (B) flakes in Figure 2.

Fig. S5. Structural and elemental characterizations of Mo₅N₆.

Fig. S6. TEM images of Mo₅N₆ sample under 200 keV electron beam.

Fig. S7. EDS spectrum of Mo₅N₆.

Fig. S8. Optical, AFM and SEM images of chemical transformation on a 4-layer MoS₂ flake.

Fig. S9. Optical images of Mo₅N₆ flakes prepared from chemical transformations at different conditions.

Fig. S10. Optical images and Raman spectra of a partially converted flake at 700 °C.

Fig. S11. Stability test of Mo₅N₆, W₅N₆ and TiN.

Fig. S12. Optical and SEM images of WS₂, W₅N₆, TiS₂ and TiN flakes.

Fig. S13. Optical and AFM image of Mo₅N₆ transport device

Fig. S14. TEM and EDS characterizations of W₅N₆ converted from WS₂.

REFERENCES AND NOTES

1. L. E. Toth, *Transition Metal Carbides and Nitrides* (Academic Press, New York, 1971).
2. H. A. Pierson, *Handbook of Refractory Carbides and Nitrides* (Noyes, Westwood, NJ, 1996).
3. M. Naguib *et al.*, Two-Dimensional Nanocrystals Produced by Exfoliation of Ti_3AlC_2 . *Advanced Materials*. **23**, 4248–4253 (2011).
4. M. R. Lukatskaya *et al.*, Cation Intercalation and High Volumetric Capacitance of Two-Dimensional Titanium Carbide. *Science*. **341**, 1502–1505 (2013).
5. B. Anasori, M. R. Lukatskaya, Y. Gogotsi, 2D metal carbides and nitrides (MXenes) for energy storage. *Nature Reviews Materials*. **2**, 16098 (2017).
6. K. Hantanasirisakul, Y. Gogotsi, Electronic and Optical Properties of 2D Transition Metal Carbides and Nitrides (MXenes). *Advanced Materials*. **30**, 1804779 (2018).
7. P. Urbankowski, B. Anasori, T. Makaryan, D. Er, S. Kota, P. L. Walsh, M. Zhao, V. B. Shenoy, M. W. Barsoum, Y. Gogotsi, Synthesis of two-dimensional titanium nitride Ti_4N_3 (MXene). *Nanoscale*. **8**, 11385–11391 (2016).
8. B. Soundiraraju, B. K. George, Two-Dimensional Titanium Nitride (Ti_2N) MXene: Synthesis, Characterization, and Potential Application as Surface-Enhanced Raman Scattering Substrate. *ACS Nano*. **11**, 8892–8900 (2017).
9. P. Urbankowski *et al.*, 2D molybdenum and vanadium nitrides synthesized by ammoniation of 2D transition metal carbides (MXenes). *Nanoscale*. **9**, 17722–17730 (2017).
10. M. Naguib, O. Mashtalir, J. Carle, V. Presser, J. Lu, L. Hultman, Y. Gogotsi, M. W. Barsoum, Two-dimensional transition metal carbides. *ACS Nano* **6**, 1322–1331 (2012).
11. B. Anasori, Y. Xie, M. Beidaghi, J. Lu, B. C. Hosler, L. Hultman, P. R. C. Kent, Y. Gogotsi, M. W. Barsoum, Two-dimensional, ordered, double transition metals carbides (MXenes). *ACS Nano* **9**, 9507–9516 (2015).
12. A. Lipatov, M. Alhabeb, M. R. Lukatskaya, A. Boson, Y. Gogotsi, A. Sinitskii, Effect of synthesis on quality, electronic properties and environmental stability of individual monolayer Ti_3C_2 MXene flakes. *Adv. Electron. Mater.* **2**, 1600255 (2016).
13. F. Shahzad, M. Alhabeb, C. B. Hatter, B. Anasori, S. Man Hong, C. M. Koo, Y. Gogotsi, Electromagnetic interference shielding with 2D transition metal carbides (MXenes). *Science*. **353**, 1137–1140 (2016).
14. Y.-Y. Peng, B. Akuzum, N. Kurra, M.-Q. Zhao, M. Alhabeb, B. Anasori, E. C. Kumbur, H. N. Alshareef, M.-D. Ger, Y. Gogotsi, All-MXene (2D titanium carbide) solid-state microsupercapacitors for on-chip energy storage. *Energy Environ. Sci.* **9**, 2847–2854 (2016).

15. H. Jin, X. Liu, A. Vasileff, Y. Jiao, Y. Zhao, Y. Zheng, S.-Z. Qiao, Single-Crystal Nitrogen-Rich Two-Dimensional Mo₅N₆ Nanosheets for Efficient and Stable Seawater Splitting. *ACS Nano*. **12**, 12761–12769 (2018).
16. L. H. Karlsson, J. Birch, J. Halim, M. W. Barsoum, P. O. Å. Persson, Atomically Resolved Structural and Chemical Investigation of Single MXene Sheets. *Nano Lett.* **15**, 4955–4960 (2015).
17. X. Sang, Y. Xie, M.-W. Lin, M. Alhabeb, K. L. Van Aken, Y. Gogotsi, P. R. C. Kent, K. Xiao, R. R. Unocic, Atomic Defects in Monolayer Titanium Carbide (Ti₃C₂T_x) MXene. *ACS Nano*. **10**, 9193–9200 (2016).
18. L. Yu, Y.-H. Lee, X. Ling, E. J. G. Santos, Y. C. Shin, Y. Lin, M. Dubey, E. Kaxiras, J. Kong, H. Wang, T. Palacios, Graphene/MoS₂ Hybrid Technology for Large-Scale Two-Dimensional Electronics. *Nano Letters*. **14**, 3055–3063 (2014).
19. Y.-C. Lin, B. Jariwala, B. M. Bersch, K. Xu, Y. Nie, B. Wang, S. M. Eichfeld, X. Zhang, T. H. Choudhury, Y. Pan, R. Addou, C. M. Smyth, J. Li, K. Zhang, M. A. Haque, S. Fölsch, R. M. Feenstra, R. M. Wallace, K. Cho, S. K. Fullerton-Shirey, J. M. Redwing, J. A. Robinson, Realizing Large-Scale, Electronic-Grade Two-Dimensional Semiconductors. *ACS Nano*. **12**, 965–975 (2018).
20. X. Li, W. Cai, J. An, S. Kim, J. Nah, D. Yang, R. Piner, A. Velamakanni, I. Jung, E. Tutuc, S. K. Banerjee, L. Colombo, R. S. Ruoff, Large-Area Synthesis of High-Quality and Uniform Graphene Films on Copper Foils. *Science*. **324**, 1312–1314 (2009).
21. X. Ling, Y.-H. Lee, Y. Lin, W. Fang, L. Yu, M. S. Dresselhaus, J. Kong, Role of the Seeding Promoter in MoS₂ Growth by Chemical Vapor Deposition. *Nano Letters*. **14**, 464–472 (2014).
22. Z. Cai, B. Liu, X. Zou, H.-M. Cheng, Chemical Vapor Deposition Growth and Applications of Two-Dimensional Materials and Their Heterostructures. *Chem. Rev.* **118**, 6091–6133 (2018).
23. S. T. Oyama, The Chemistry of Transition Metal Carbides and Nitrides, S. T. Oyama, Ed. (Blackie Academic and Professional, London, 1996).
24. C. Giordano, C. Erpen, W. Yao, M. Antonietti, Synthesis of Mo and W Carbide and Nitride Nanoparticles via a Simple “Urea Glass” Route. *Nano Letters*. **8**, 4659–4663 (2008).
25. J. Liu, S. Tang, Y. Lu, G. Cai, S. Liang, W. Wang, X. Chen, Synthesis of Mo₂N nanolayer coated MoO₂ hollow nanostructures as high-performance anode materials for lithium-ion batteries. *Energy & Environmental Science*. **6**, 2691 (2013).
26. M. B. Sreedhara, K. Vasu, C. N. R. Rao, Synthesis and Characterization of Few-layer Nanosheets of GaN and Other Metal Nitrides. *Zeitschrift für anorganische und allgemeine Chemie*. **640**, 2737–2741 (2014).

27. G.-D. Sun, G.-H. Zhang, K.-C. Chou, Synthesis of molybdenum nitrides nanosheets by nitriding 2H-MoS₂ with ammonia. *Journal of the American Ceramic Society*. **101**, 2796–2808 (2018).
28. X. Xiao, H. Wang, P. Urbankowski, Y. Gogotsi, Topochemical synthesis of 2D materials. *Chemical Society Reviews*. **47**, 8744–8765 (2018).
29. K. S. Novoselov, D. Jiang, F. Schedin, T. J. Booth, V. V. Khotkevich, S. V. Morozov, A. K. Geim, Two-dimensional atomic crystals. *Proceedings of the National Academy of Sciences of the United States of America*. **102**, 10451–10453 (2005).
30. K. Kang, S. Xie, L. Huang, Y. Han, P. Y. Huang, K. F. Mak, C.-J. Kim, D. Muller, J. Park, High-mobility three-atom-thick semiconducting films with wafer-scale homogeneity. *Nature*. **520**, 656–660 (2015).
31. S. D. Yim, S. J. Kim, J. H. Baik, I. Nam, Y. S. Mok, J.-H. Lee, B. K. Cho, S. H. Oh, Decomposition of Urea into NH₃ for the SCR Process. *Industrial & Engineering Chemistry Research*. **43**, 4856–4863 (2004).
32. A. Lundström, B. Andersson, L. Olsson, Urea thermolysis studied under flow reactor conditions using DSC and FT-IR. *Chemical Engineering Journal*. **150**, 544–550 (2009).
33. A. Splendiani, L. Sun, Y. Zhang, T. Li, J. Kim, C.-Y. Chim, G. Galli, F. Wang, Emerging Photoluminescence in Monolayer MoS₂. *Nano Letters*. **10**, 1271–1275 (2010).
34. T. J. Wieting, J. L. Verble, Infrared and Raman Studies of Long-Wavelength Optical Phonons in Hexagonal MoS₂. *Physical Review B*. **3**, 4286–4292 (1971).
35. J. L. Verble, T. J. Wieting, Lattice Mode Degeneracy in MoS₂ and Other Layer Compounds. *Physical Review Letters*. **25**, 362–365 (1970).
36. G. Eda, H. Yamaguchi, D. Voiry, T. Fujita, M. Chen, M. Chhowalla, Photoluminescence from Chemically Exfoliated MoS₂. *Nano Letters*. **11**, 5111–5116 (2011).
37. A. Garcia, A. M. Raya, M. M. Mariscal, R. Esparza, M. Herrera, S. I. Molina, G. Scavello, P. L. Galindo, M. Jose-Yacaman, A. Ponce, Analysis of electron beam damage of exfoliated MoS₂ sheets and quantitative HAADF- STEM imaging. *Ultramicroscopy*. **146**, 33–38 (2014).
38. R. Zan, Q. M. Ramasse, R. Jalil, T. Georgiou, U. Bangert, K. S. Novoselov, Control of Radiation Damage in MoS₂ by Graphene Encapsulation. *ACS Nano*. **7**, 10167–10174 (2013).
39. L. Zhang, X. Ji, X. Ren, Y. Ma, X. Shi, Z. Tian, A. M. Asiri, L. Chen, B. Tang, X. Sun, Electrochemical Ammonia Synthesis via Nitrogen Reduction Reaction on a MoS₂ Catalyst: Theoretical and Experimental Studies. *Advanced Materials*. **30**, 1800191 (2018).
40. C. Martella, P. Melloni, E. Cinquanta, E. Cianci, M. Alia, M. Longo, A. Lamperti, S. Vangelista, M. Fanciulli, A. Molle, Engineering the Growth of MoS₂ via Atomic Layer

Deposition of Molybdenum Oxide Film Precursor. *Advanced Electronic Materials*. **2**, 1600330 (2016).

41. E. S. Kadantsev, P. Hawrylak, Electronic structure of a single MoS₂ monolayer. *Solid State Communications*. **152**, 909–913 (2012).
42. A. Yu. Ganin, L. Kienle, G. V. Vajenine, Synthesis and characterisation of hexagonal molybdenum nitrides. *Journal of Solid State Chemistry*. **179**, 2339–2348 (2006).
43. F. Bonaccorso, Z. Sun, T. Hasan, A. C. Ferrari, Graphene photonics and optoelectronics. *Nature Photonics*. **4**, 611–622 (2010).
44. M. Thirupanthaka, R. V. Kashid, C. Sekhar Rout, D. J. Late, Temperature dependent Raman spectroscopy of chemically derived few layer MoS₂ and WS₂ nanosheets. *Applied Physics Letters*. **104**, 081911 (2014).
45. C. J. Carmalt, S. A. O'Neill, I. P. Parkin, E. S. Peters, Titanium sulfide thin films from the aerosol-assisted chemical vapour deposition of [Ti(SBu^t)₄]. *Journal of Materials Chemistry*. **14**, 830–834 (2004).
46. C. C. Chen, N. T. Liang, W. S. Tse, I. Y. Chen, J. G. Duh, Raman Spectra of Titanium Nitride Thin Films. *Chinese Journal of Physics*. **32**, 205 (1994).
47. S. Yu, Q. Zeng, A. R. Oganov, G. Frapper, L. Zhang, Phase stability, chemical bonding and mechanical properties of titanium nitrides: a first-principles study. *Phys. Chem. Chem. Phys.* **17**, 11763–11769 (2015).
48. Z. Zhao, K. Bao, D. Duan, F. Tian, Y. Huang, H. Yu, Y. Liu, B. Liu, T. Cui, The low coordination number of nitrogen in hard tungsten nitrides: a first-principles study. *Physical Chemistry Chemical Physics*. **17**, 13397–13402 (2015).
49. V. Grillo, E. Rotunno, STEM_CELL: A software tool for electron microscopy: Part I—simulations. *Ultramicroscopy*. **125**, 97–111 (2013).

Acknowledgments: X. L. acknowledges the support of Boston University and Boston University Photonics Center. The device fabrication was done in Professor Kenneth Burch's lab at Boston College. Electrical measurements were conducted at MIT. Y. L. and T. P. acknowledge the partial support by the U.S. Army Research Office through the Institute for Soldier Nanotechnologies, under Cooperative Agreement number W911NF-18-2-0048, AFOSR FATE MURI, grant no. FA9550-15-1-0514, and the STC Center for Integrated Quantum Materials, NSF grant no. DMR

1231319. The TEM imaging was performed at the Center for Nanoscale Systems (CNS), a member of the National Nanotechnology Coordinated Infrastructure Network (NNCI), which is supported by the National Science Foundation under NSF award no. 1541959. CNS is part of Harvard University. **Author Contributions:** J.C., T.L. and X.L. conceived and designed the experiments. J.C. and H.G. performed the conversion, optical characterization and Raman measurements. T.L. performed TEM, STEM and AFM measurements. T.L. fabricated device. T.L. X.W. and Y.L. conducted electrical measurements supervised by X.L. and T.P. H.W. conducted XPS measurements. J.C., T.L. and X.L. analyzed the data and wrote the manuscript together with input from all authors. **Competing interests:** The authors declare that they have no competing interests. **Data and materials availability:** All data supporting the stated conclusions of the manuscript are in the paper and/or in the Supplementary Materials. Additional data related to this paper may be requested from the authors.

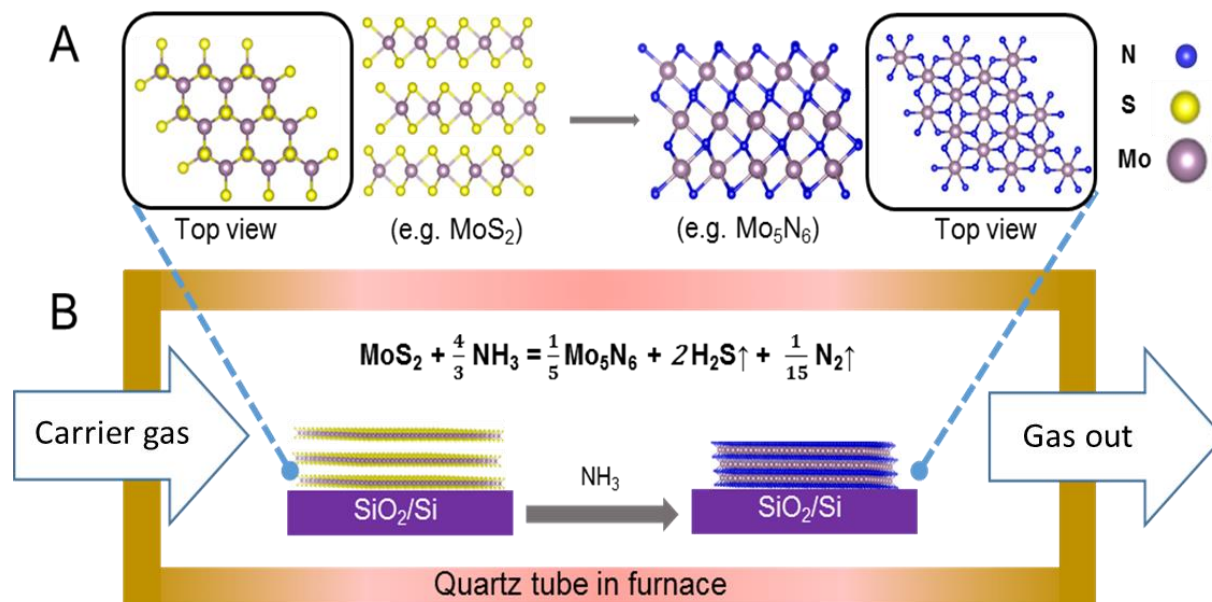


Fig. 1. Schematic illustration of chemical conversion from MoS₂ to Mo₅N₆. (A) Structural changes from MoS₂ to Mo₅N₆. (B) Schematics of the experimental setup for chemical conversion reactions.

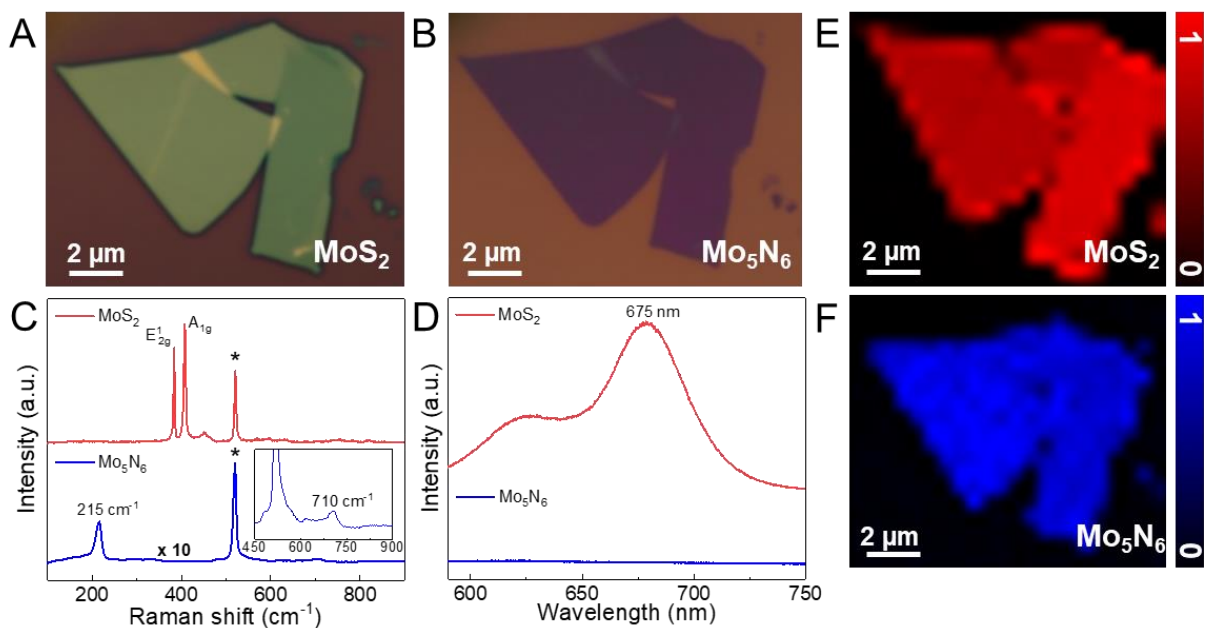


Fig. 2. Typical optical microscope, Raman spectroscopy and PL characterization of MoS₂ and Mo₅N₆ flakes. (A) Optical images of MoS₂ exfoliated on SiO₂/Si substrate. (B) Optical image of Mo₅N₆ converted from MoS₂ in (A). (C) Comparison of Raman spectra of MoS₂ and Mo₅N₆. Peaks labeled with “*” are from the SiO₂/Si substrate. (D) Comparison of PL spectra of MoS₂ and Mo₅N₆. (E and F) Raman intensity maps of the A_{1g} mode of MoS₂ (E) and the 215 cm⁻¹ mode of Mo₅N₆ (F), respectively. Color bars show normalized Raman intensities, where “1” represent and “0” represent maximum and minimum intensity of Raman modes, respectively.

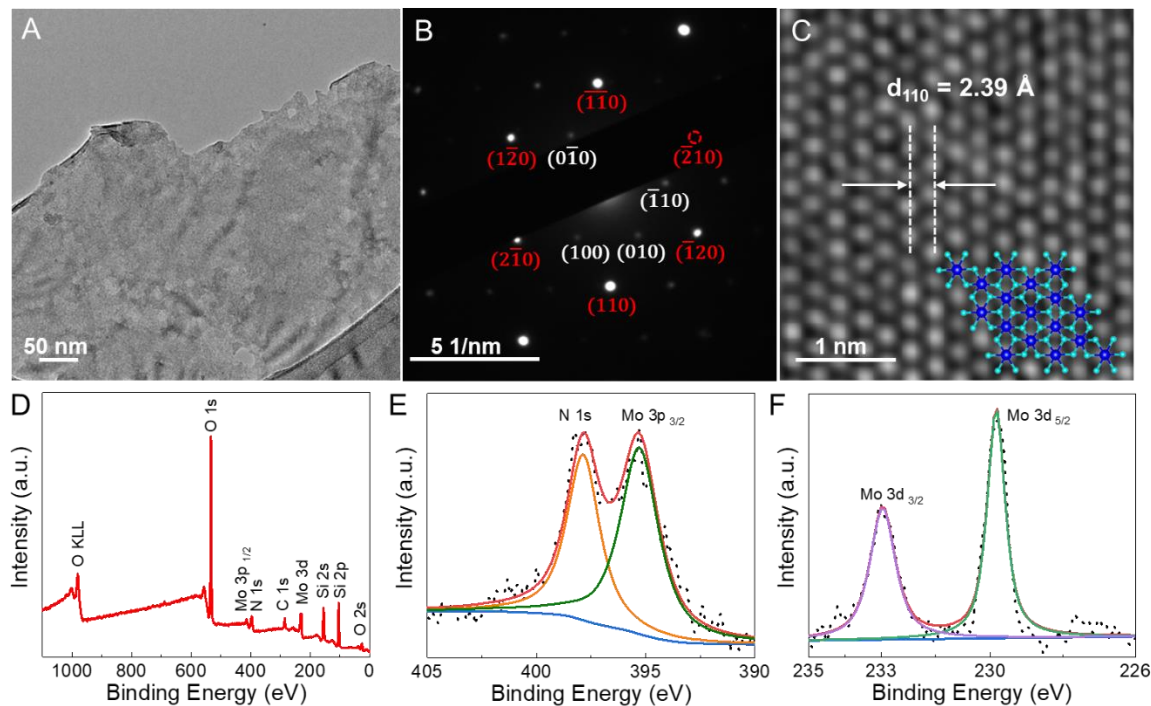


Fig. 3. Crystal structure and elemental analysis of Mo_5N_6 samples converted from MoS_2 . (A) Low magnification TEM image of Mo_5N_6 . (B) SAED pattern taken by a 25 cm camera. Diffraction planes are labelled according to SAED simulation in fig. S4. Red circle corresponds to a diffraction plane blocked by TEM beam stop. (C) Filtered HAADF STEM image. Hexagonal Mo pattern is clearly observed. Mo atoms and N atoms are labelled in blue and cyan color, respectively. (D) XPS survey spectrum of Mo_5N_6 . (E and F) XPS spectra of Mo_5N_6 in Mo 3p and N 1s region (E) and Mo 3d region (F).

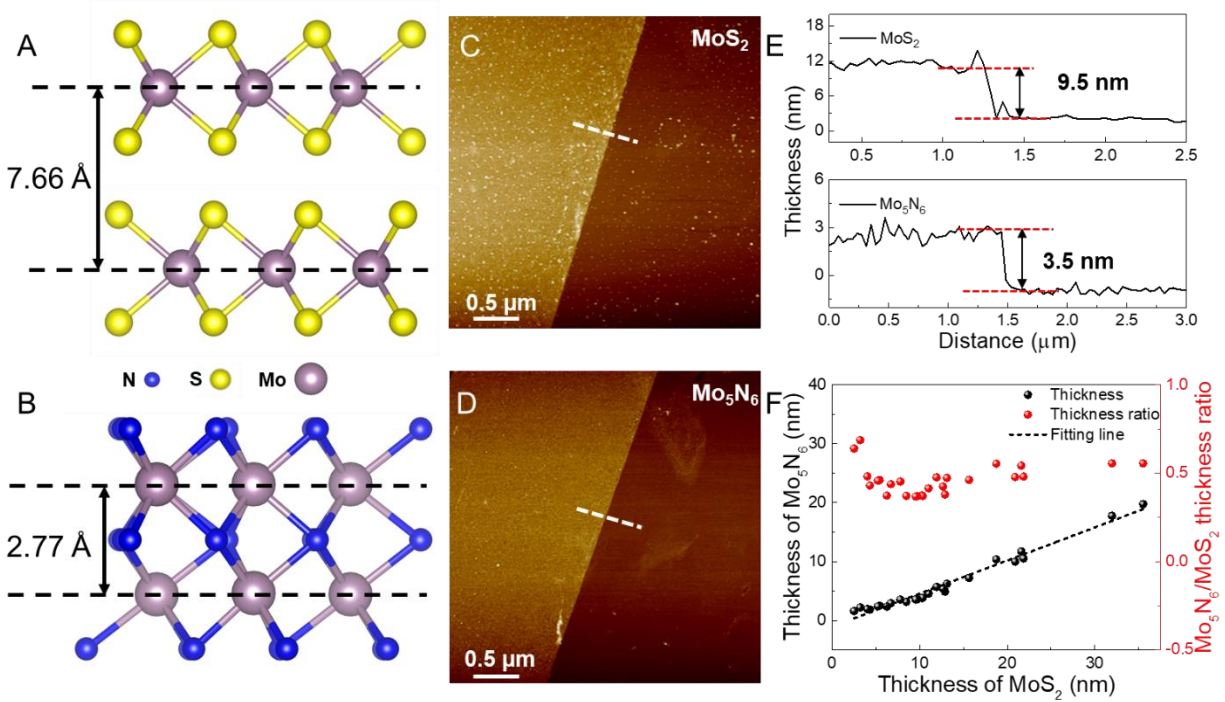


Fig. 4. Thickness characterization and analysis of samples before (MoS₂) and after conversion (Mo₅N₆). (A and B) Side view of crystal structures labeled with distance between adjacent Mo layers in MoS₂ and Mo₅N₆. (C and D) AFM images of the same flake before (MoS₂, C) and after conversion (Mo₅N₆, D). The white dashed lines indicate the location where we measured the thickness of the flakes. (E) AFM height profiles of the flake before (MoS₂, C) and after conversion (Mo₅N₆, D). (F) Correlation plot of the thickness of MoS₂ and converted Mo₅N₆ (in black). Data points in red show the corresponding thickness ratios of Mo₅N₆/MoS₂.

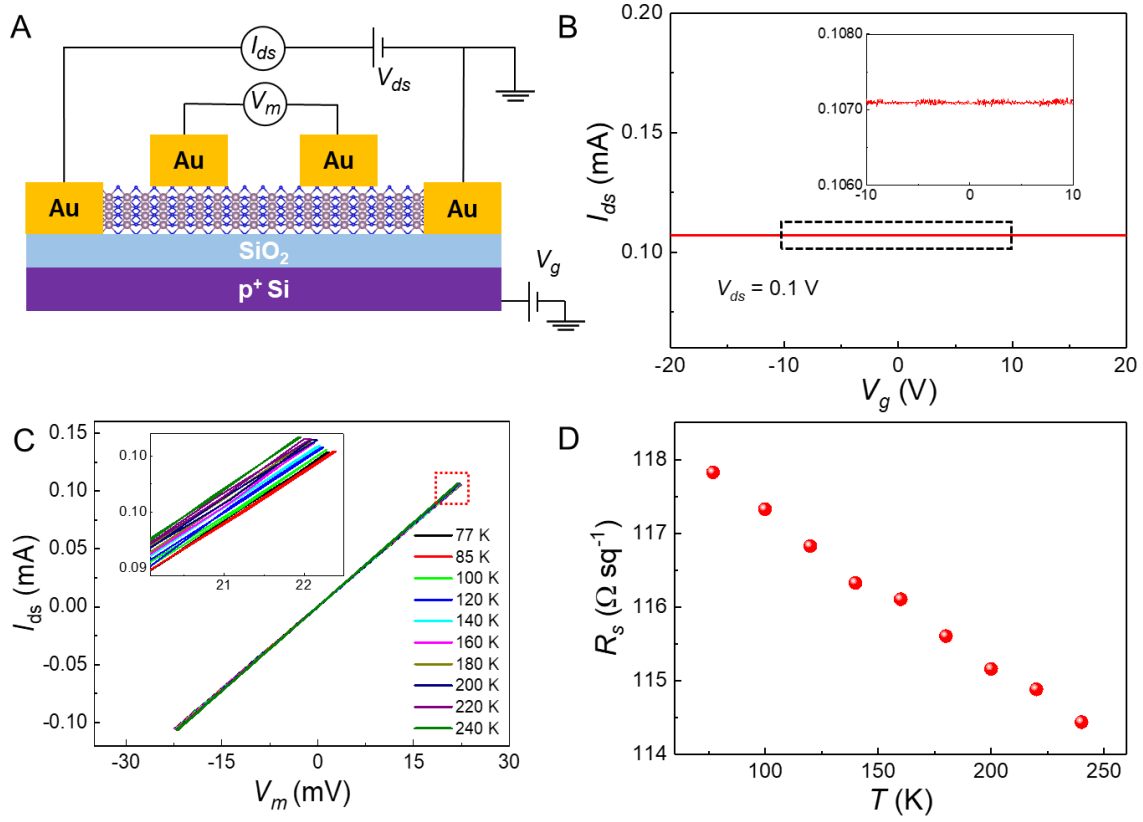


Fig. 5. Electrical transport measurements of Mo₅N₆. (A) Schematics of a back gate device together with electrical connections. (B) Transfer curve of Mo₅N₆ transport device for both forward and reverse V_g bias with back gate modulations. Inset shows a zoom in image of the area indicated by the black rectangle. Negligible gate dependence of the I_{ds} is observed in Mo₅N₆ transport device. (C) Output I - V curve of Mo₅N₆ transport device under different temperatures at zero gate voltage. Inset shows a zoom in region of the I - V curve indicated by the red square. (D) Temperature dependence of the sheet resistance of the Mo₅N₆ sample.

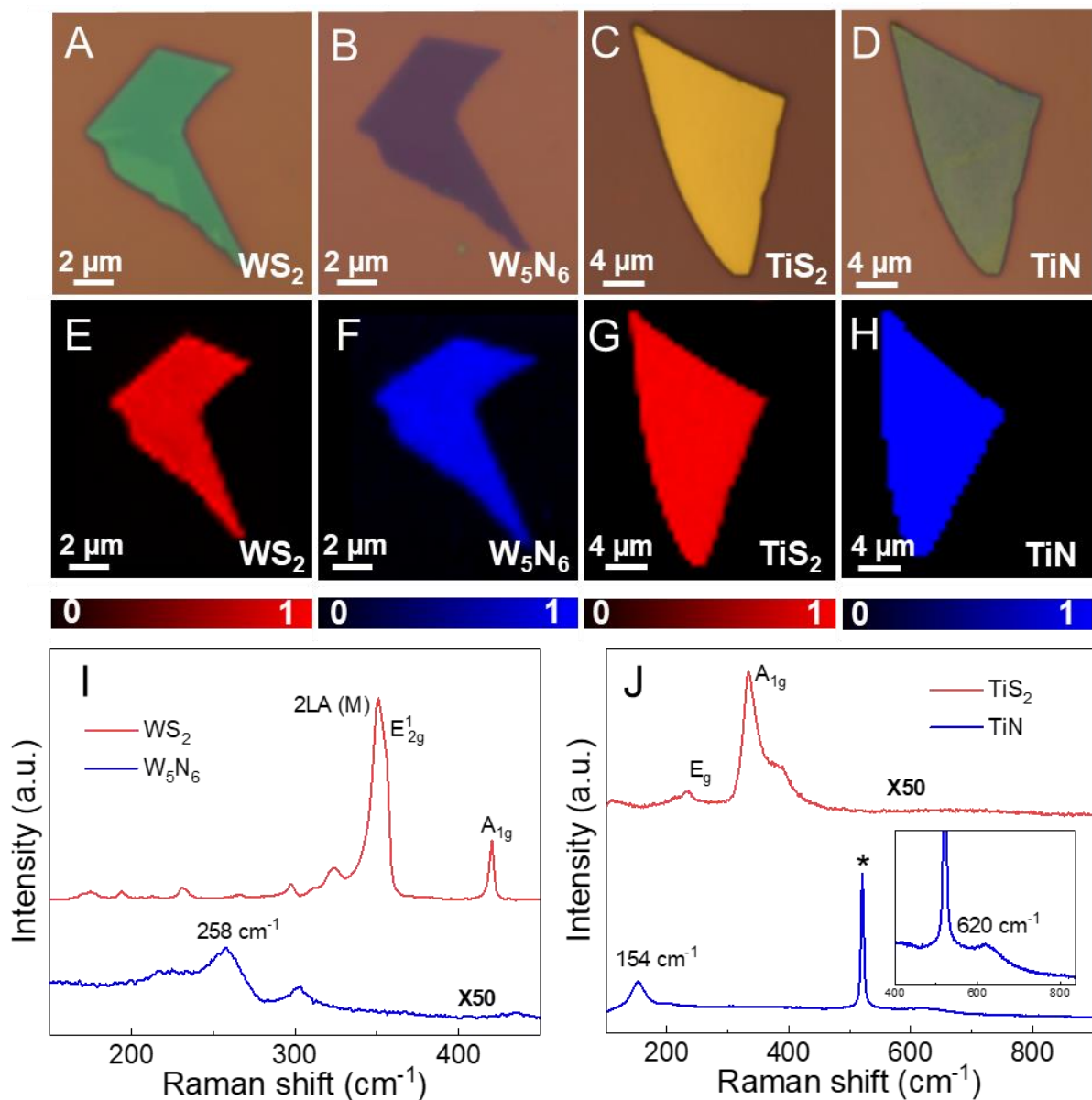


Fig. 6. Conversion on WS₂ and TiS₂ for W₅N₆ and TiN. (A to D) Optical images of WS₂ (A), W₅N₆ (B), TiS₂ (C), and TiN (D). (E to H) Raman intensity maps of E_{2g}¹ mode of WS₂ (E), 258 cm⁻¹ mode of W₅N₆ (F), A_{1g} mode of TiS₂ (G) and 154 cm⁻¹ mode of TiN (H). Color bars show normalized Raman intensities, where “1” and “0” represent maximum and minimum intensity of Raman modes, respectively. (I and J) Comparison of Raman spectra of WS₂ and W₅N₆ (I), TiS₂ and TiN (J). Peak labeled with “*” is from the SiO₂/Si substrate.

Supplementary Materials for

Realization of 2D Crystalline Metal Nitrides via Selective Atomic Substitution

Jun Cao^{1†}, Tianshu Li^{2†}, Hongze Gao², Yuxuan Lin⁴, Xingzhi Wang¹, Haozhe Wang⁴, Tomás Palacios⁴, Xi Ling^{1,2,3*}

1. Department of Chemistry, Boston University, 590 Commonwealth Avenue, Boston, MA 02215, USA.

2. Division of Materials Science and Engineering, Boston University, 15 St. Marys Street, Boston, MA 02215, USA.

3. The Photonics Center, Boston University, 8 St. Marys Street, Boston, MA 02215, USA.

4. Department of Electrical Engineering and Computer Science, Massachusetts Institute of Technology, Cambridge, MA 02139, USA.

[†]These authors contributed equally to this work.

*Corresponding author. Email: xiling@bu.edu (X.L.)

This PDF file includes:

Fig. S1. Typical optical images of MoS₂ and Mo₅N₆ flakes with different thicknesses.

Fig. S2. Absorption spectra of MoS₂ and Mo₅N₆ samples on quartz substrate.

Fig. S3. AFM images of MoS₂ and Mo₅N₆ flakes in Figure (2).

Fig. S4. Maps of PL intensity at 673 nm of MoS₂ (A) and Mo₅N₆ (B) flakes in Figure 2.

Fig. S5. Structural and elemental characterizations of Mo₅N₆.

Fig. S6. TEM images of Mo₅N₆ sample under 200 keV electron beam.

Fig. S7. EDS spectrum of Mo₅N₆.

Fig. S8. Optical, AFM and SEM images of chemical transformation on a 4-layer MoS₂ flake.

Fig. S9. Optical images of Mo₅N₆ flakes prepared from chemical transformations at different conditions.

Fig. S10. Optical images and Raman spectra of a partially converted flake at 700 °C.

Fig. S11. Stability test of Mo₅N₆, W₅N₆ and TiN.

Fig. S12. Optical and SEM images of WS₂, W₅N₆, TiS₂ and TiN flakes.

Fig. S13. Optical and AFM image of Mo₅N₆ transport device

Fig. S14. TEM and EDS characterizations of W₅N₆ converted from WS₂.

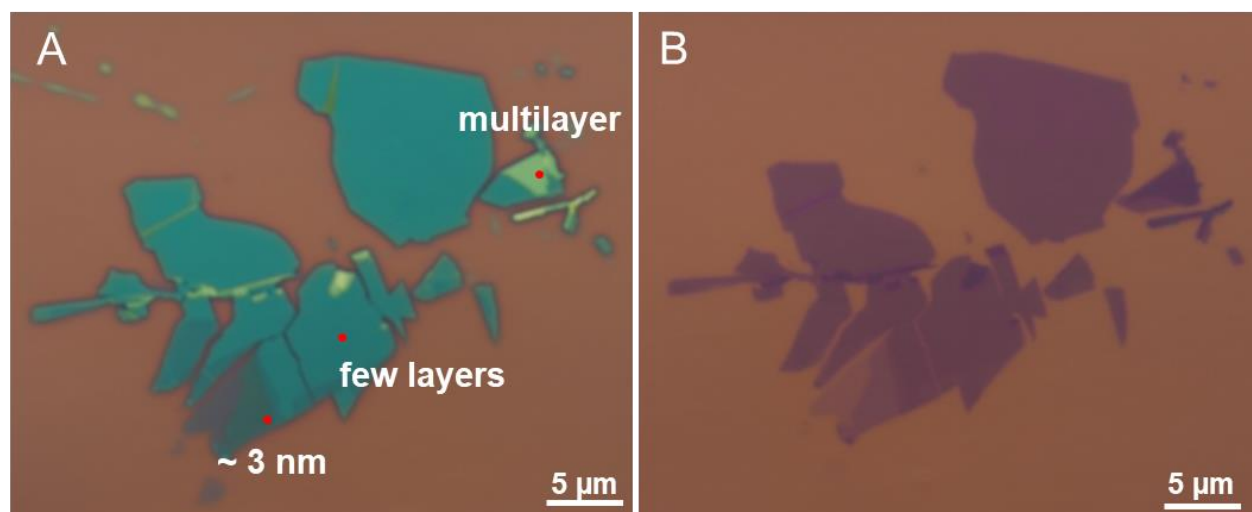


Fig. S1. Typical optical images of MoS₂ and Mo₅N₆ flakes with different thicknesses. (A)

MoS₂ flakes before the conversion. **(B)** Mo₅N₆ flakes converted from MoS₂ flakes in **(A)**.

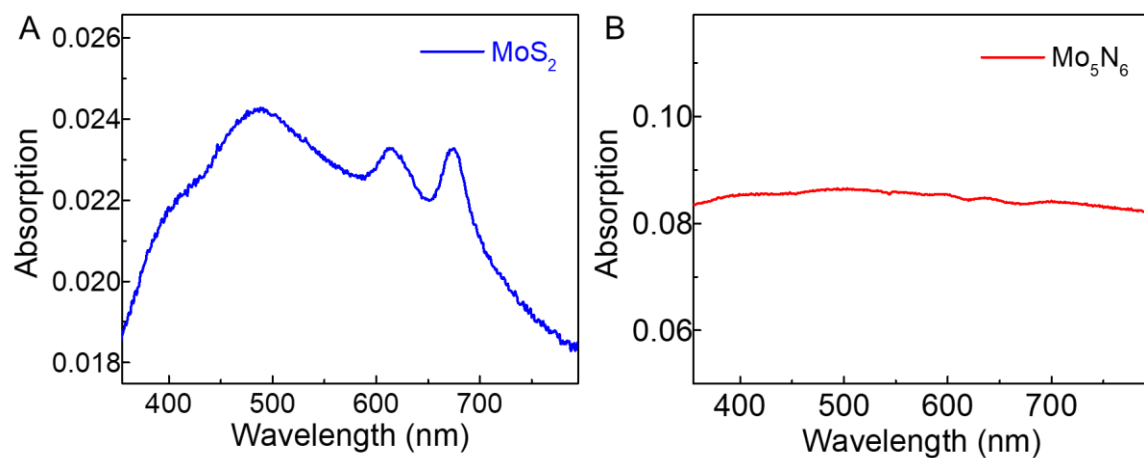


Fig. S2. Absorption spectra of MoS₂ and Mo₅N₆ samples on a quartz substrate. (A) Absorption spectrum of MoS₂ on a quartz substrate. (B) Absorption spectrum of Mo₅N₆ samples converted from MoS₂ flakes in (A) on the same quartz substrate.

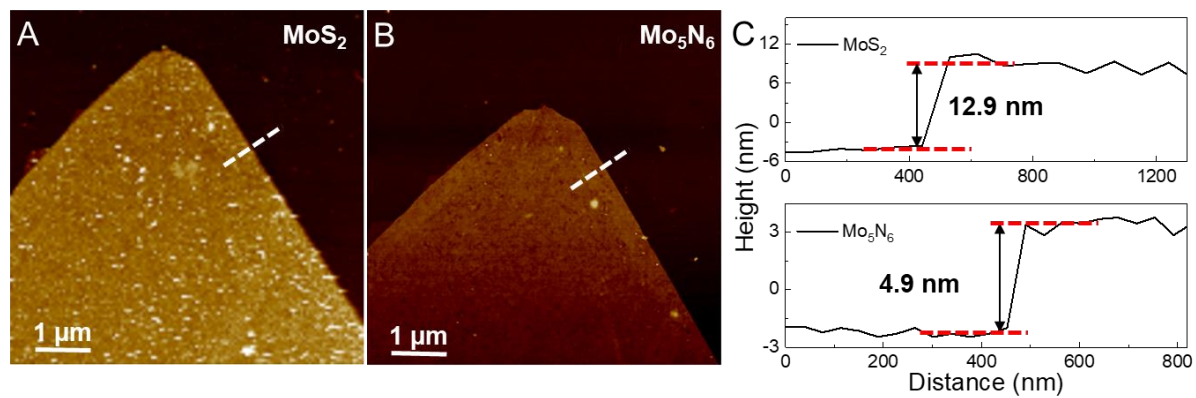


Fig. S3. AFM images of MoS₂ and Mo₅N₆ flakes in Figure (2). (A) AFM image of MoS₂ flake. (B) AFM image of Mo₅N₆ flake. White dash lines indicate the position where heights are extracted. (C) Height profiles of MoS₂ and Mo₅N₆ flakes shown in (A) and (B).

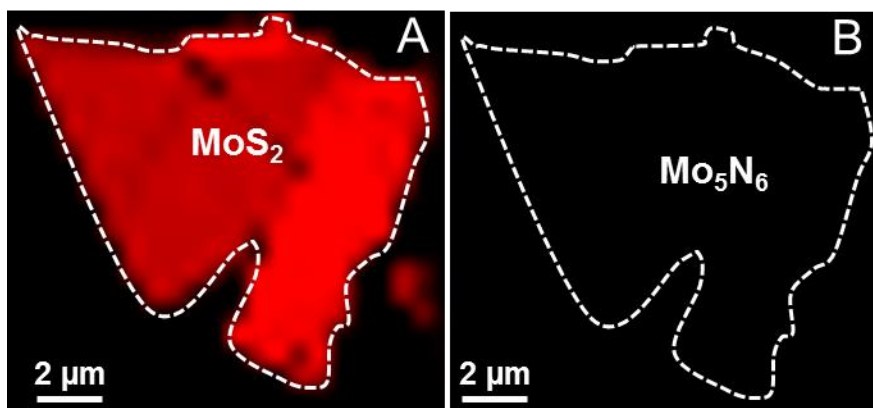


Fig. S4. Maps of PL intensity at 673 nm of MoS₂ (A) and Mo₅N₆ (B) flakes in Figure 2. The white dashed lines circle the contour of MoS₂ flakes shown in (A).

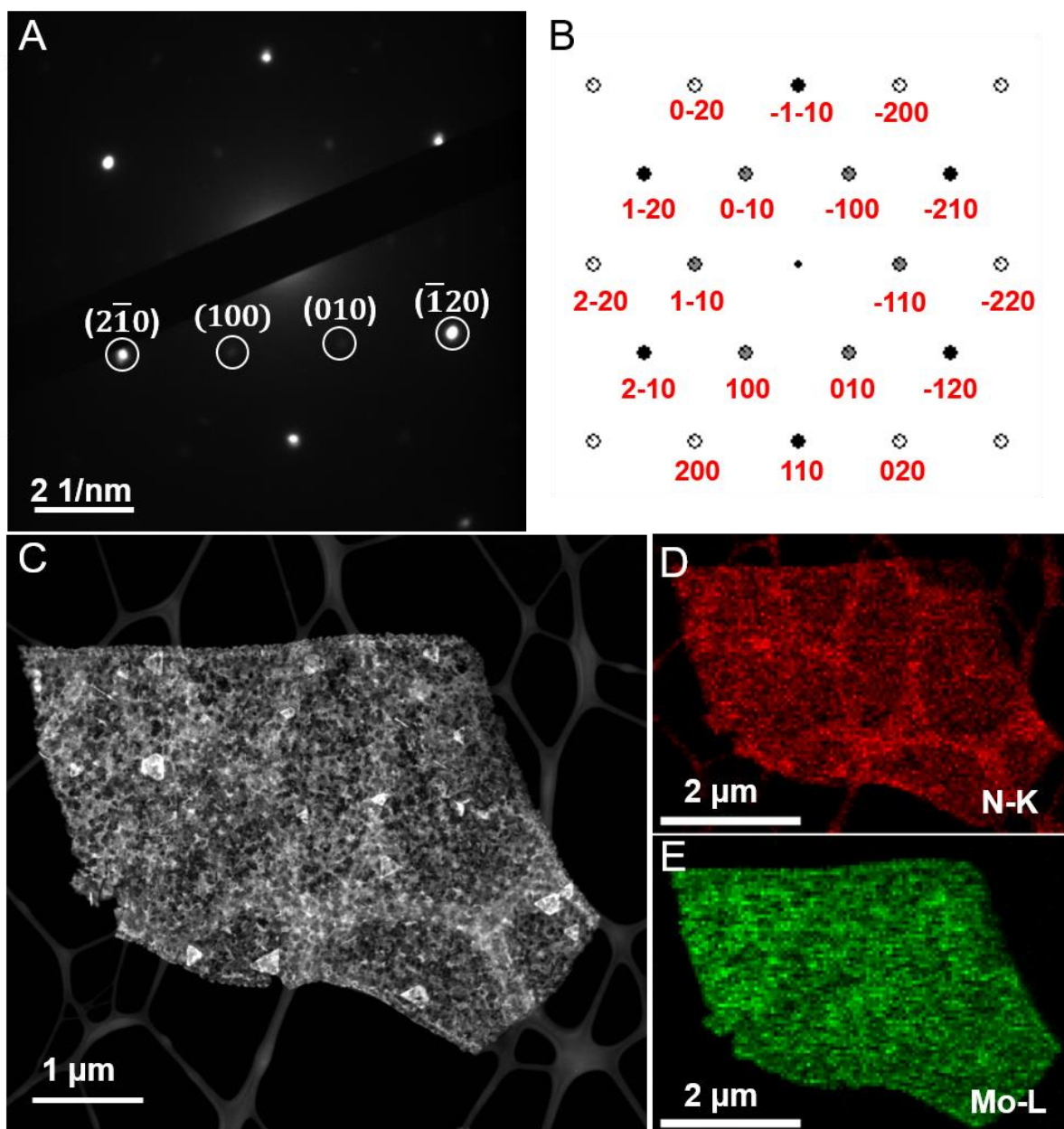


Fig. S5. Structural and elemental characterizations of Mo_5N_6 . (A) SAED pattern of Mo_5N_6 . (B) Simulated SAED pattern of Mo_5N_6 . (C) Low magnification dark field STEM image of a thick Mo_5N_6 flake. (D and E) EDS mapping of N K peak (D) and Mo L peak (E) from Mo_5N_6 flake shown in (C).

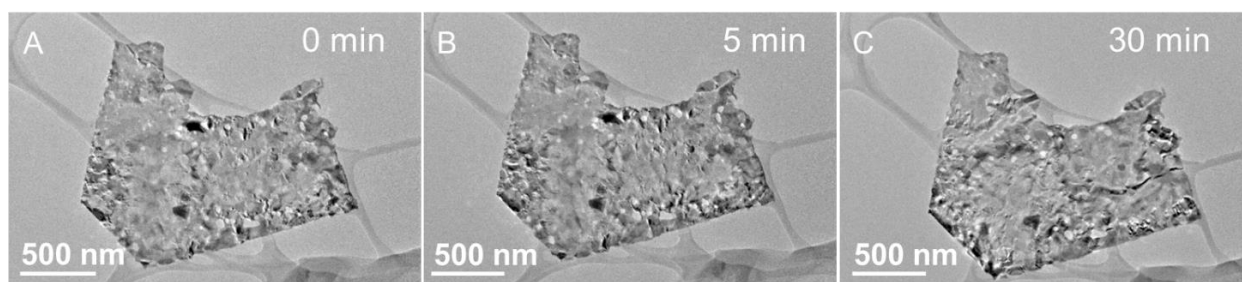


Fig. S6. TEM images of Mo₅N₆ sample under 200 keV electron beam. (A to C) TEM images of Mo₅N₆ after 0 min (A), 5 min (B) and 20 min (C) exposure under 200 keV electron beam.

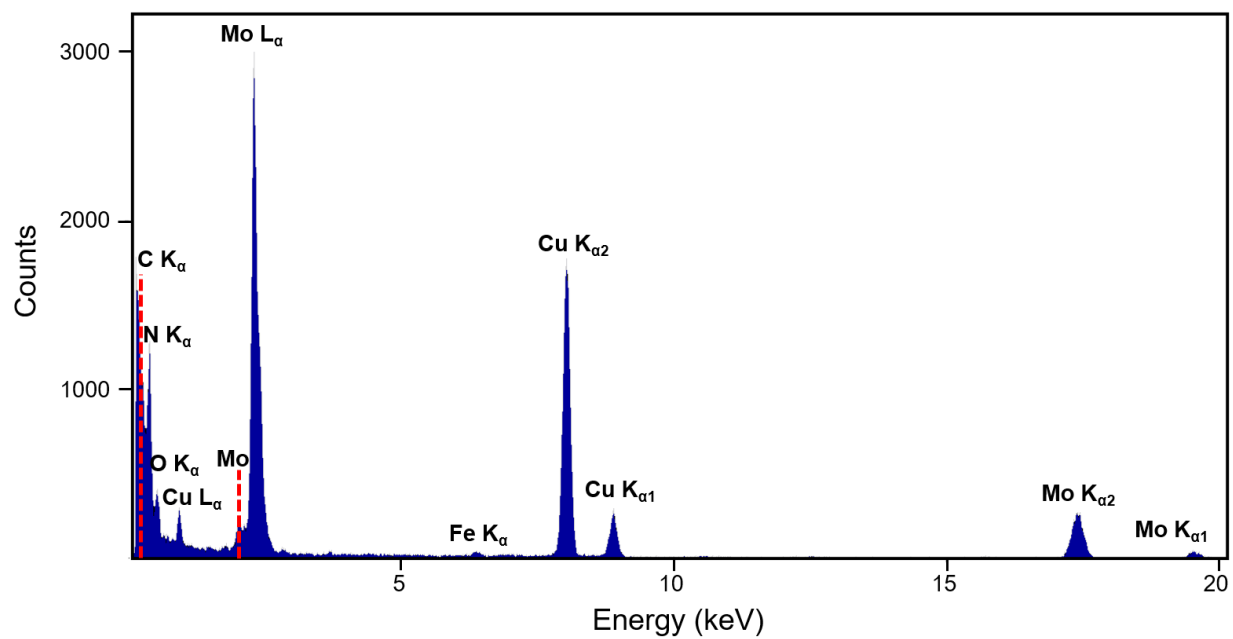


Fig. S7. EDS spectrum of Mo₅N₆. Cu and C peaks are from TEM grid. Fe peaks are from the TEM instrument.

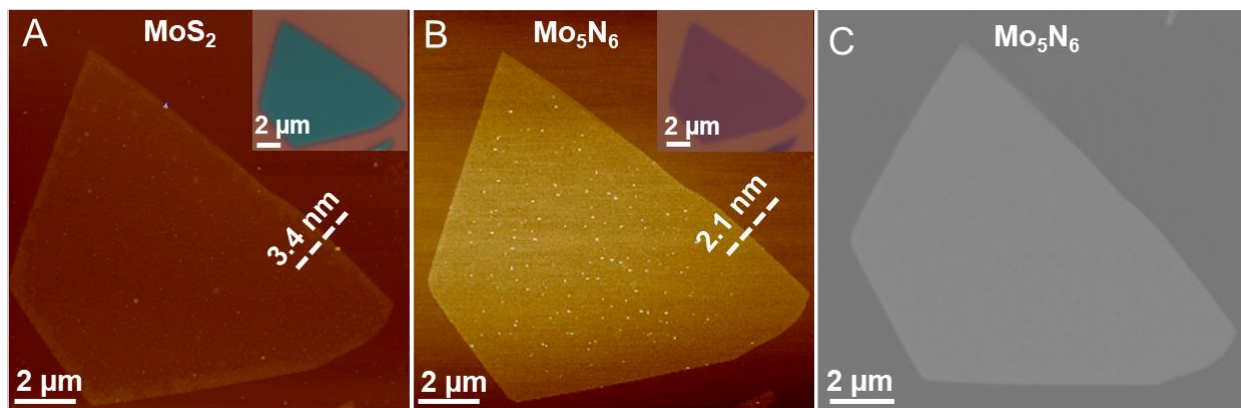


Fig. S8. Optical, AFM and SEM images of chemical transformation on a 4-layer MoS₂ flake.

(A) AFM image of MoS₂ flake. Inset: Optical image of MoS₂ flake. (B) AFM image of Mo₅N₆ flake. Inset: Optical image of Mo₅N₆ flake. White dashed lines show the location where thickness of the flakes is measured. (C) SEM image of Mo₅N₆ flake. AFM and SEM images show smooth surface after chemical transformation.

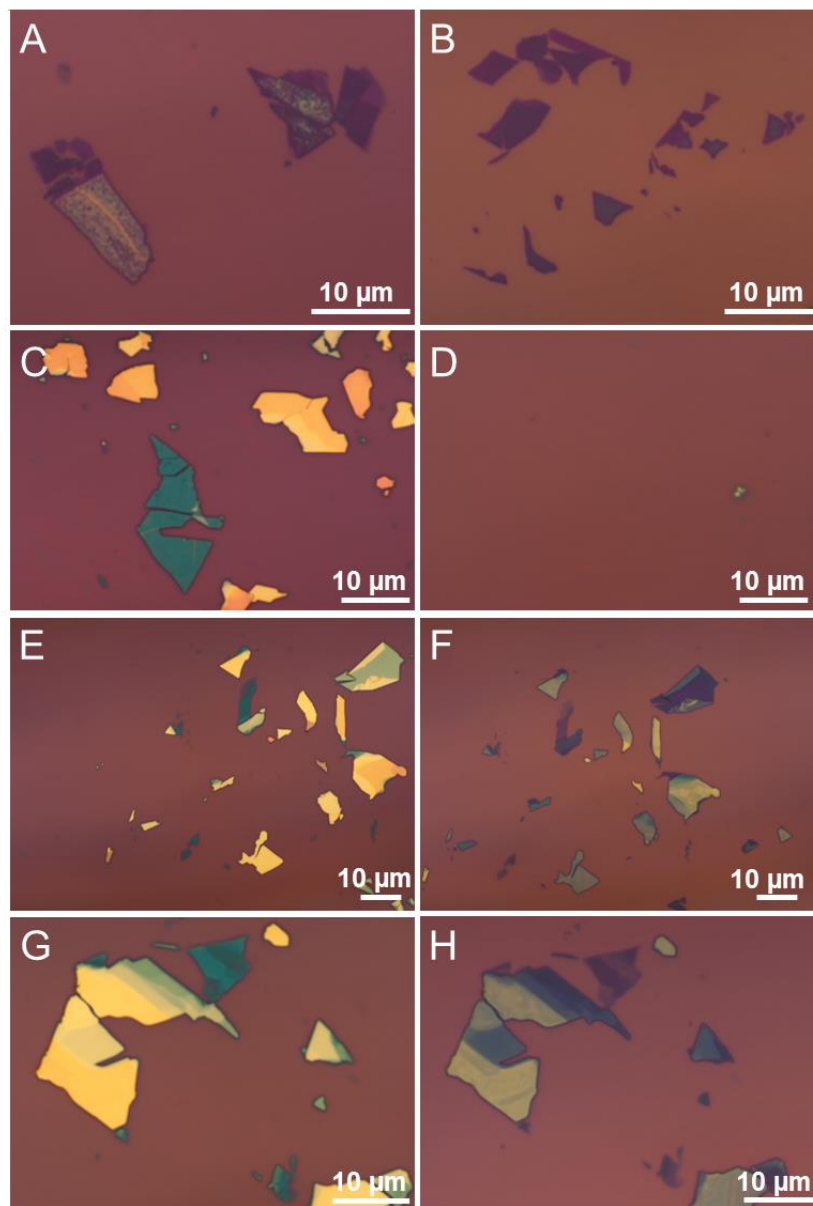


Fig. S9. Optical images of Mo₅N₆ flakes prepared from chemical transformations at different conditions. (A) Optical images of Mo₅N₆ samples converted with 100 mg urea. (B) Optical images of Mo₅N₆ samples converted with 500 mg urea. (C and D) Optical images of samples before (C) and after (D) conversion without urea. (E and F) Optical images of samples before (E) and after conversion (F) at 800 °C with 500 mg urea. (G and H) Optical images of samples before (G) and after conversion (H) at 750 °C with 500 mg urea.

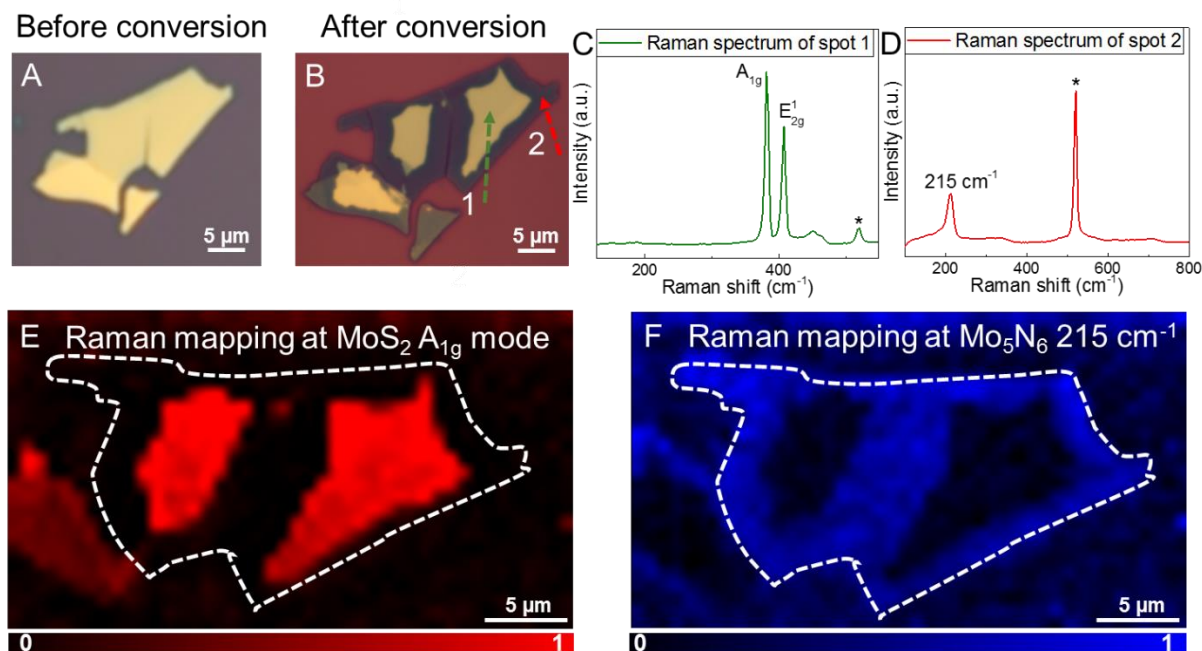


Fig. S10. Optical images and Raman spectra of a partially converted flake at 700 °C. (A and B) Optical images of flake before conversion-MoS₂ (A) and after conversion-Mo₅N₆ (B). (C and D) Raman spectra of flake after partial conversion at spot 1 (C) and spot 2 (D). Peak labeled with * is from SiO₂/Si substrate. (E and F) Raman mappings of the flake at MoS₂ A_{1g} mode (E) and Mo₅N₆ 214 cm⁻¹(F). The white dashed lines circle the contour of MoS₂ flakes shown in (B).

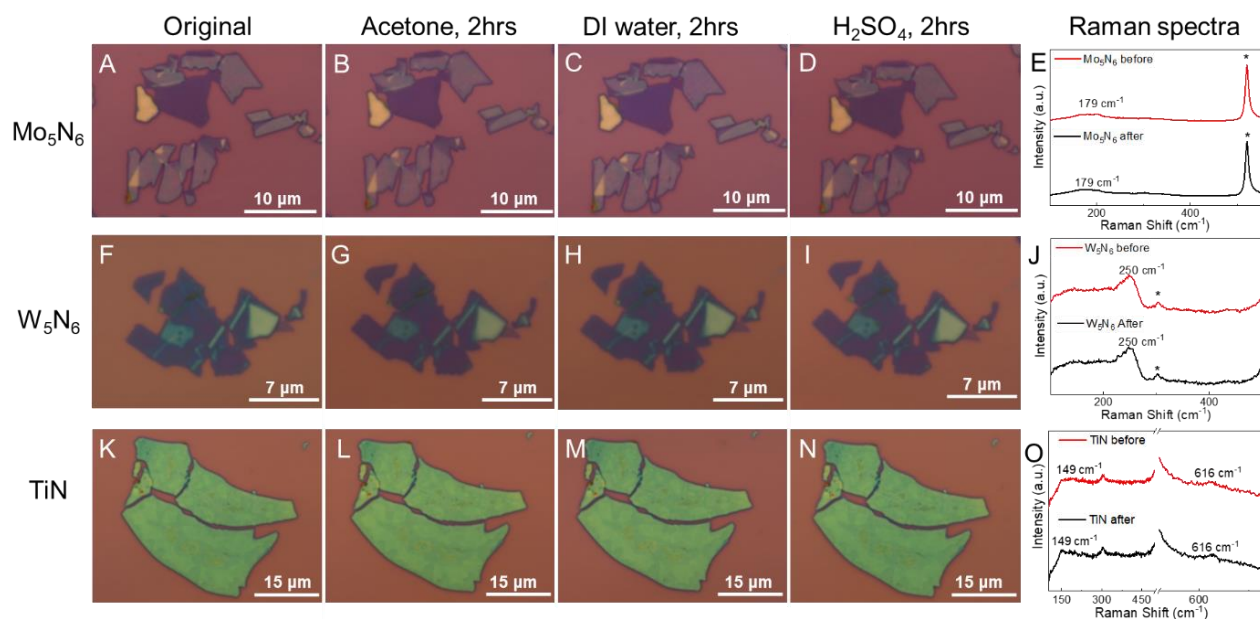


Fig.S11. Stability test of Mo₅N₆, W₅N₆ and TiN. (A to D) Optical images of Mo₅N₆ flakes before any treatment (A), after two-hour immersion in acetone (B), after two-hour immersion in deionized water (C), and after two-hour immersion in 1mol/L H₂SO₄ solution (D). (E) Raman spectra of a typical Mo₅N₆ sample before and after the stability tests. (F to I) Optical images of W₅N₆ flakes before any treatment (F), after two-hour immersion in acetone (G), after two-hour immersion in deionized water (H), and after two-hour immersion in 1mol/L H₂SO₄ solution (I). (J) Raman spectra of a typical W₅N₆ sample before and after the stability tests. (K to O) Optical images of TiN flakes before any treatment (K), after two-hour immersion in acetone (L), after two-hour immersion in deionized water (M), and after two-hour immersion in 1mol/L H₂SO₄ solution (N). (O) Raman spectra of a typical TiN sample before and after the stability tests.

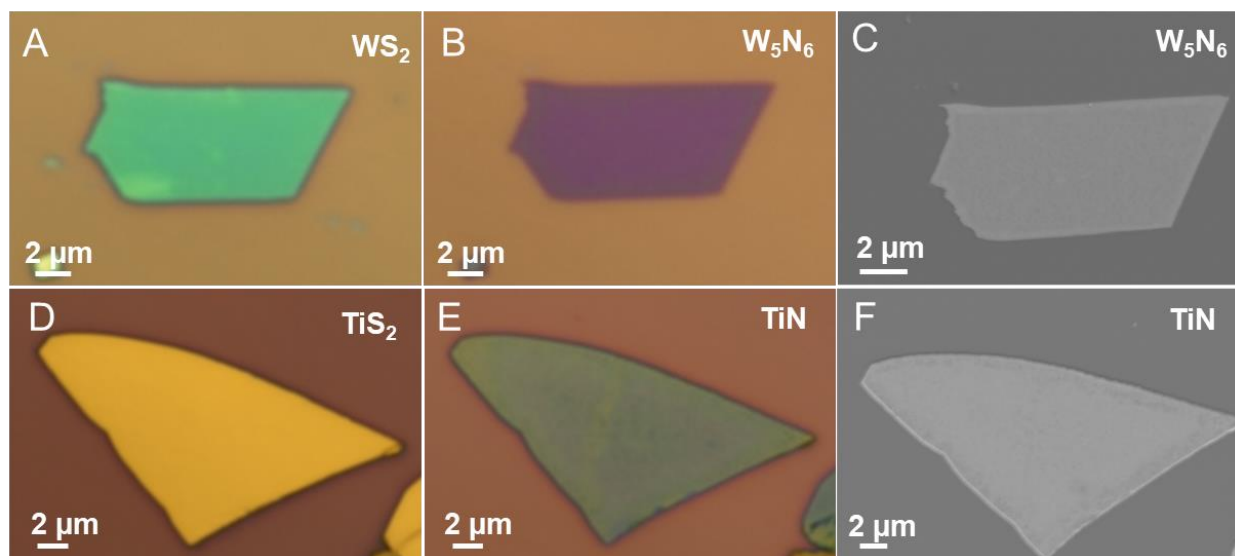


Fig. S12. Optical and SEM images of WS₂, W₅N₆, TiS₂, and TiN flakes. (A) Optical image of a WS₂ flake. (B) Optical image of a W₅N₆ flake. (C) SEM image of a W₅N₆ flake. (D) Optical image of a TiS₂ flake. (E) Optical image of a Mo₅N₆ flake. (F) SEM image of a TiN flake.

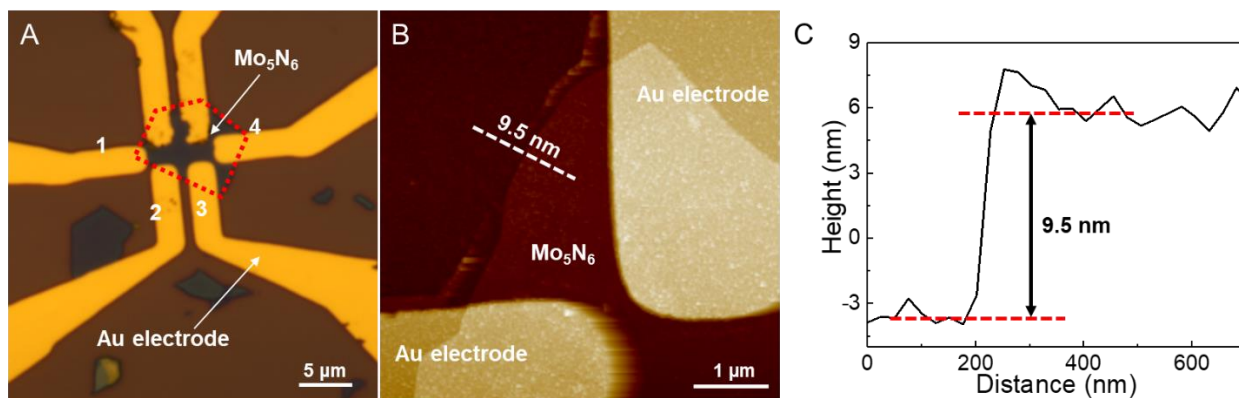


Fig. S13. Optical and AFM images of Mo₅N₆ transport device. (A) Optical image of a 6-terminal transport device of Mo₅N₆. Area circled by the red curve is the Mo₅N₆ flake that is used for device. Au electrodes from 1 to 4 are labelled and used for 4-probe electrical measurements. (B) AFM image of the Mo₅N₆ transport device. The thickness of the flake is ~ 9.5 nm. White dashed line indicated the location where thickness was extracted. (C) Height profile of Mo₅N₆ flake in the transport device.

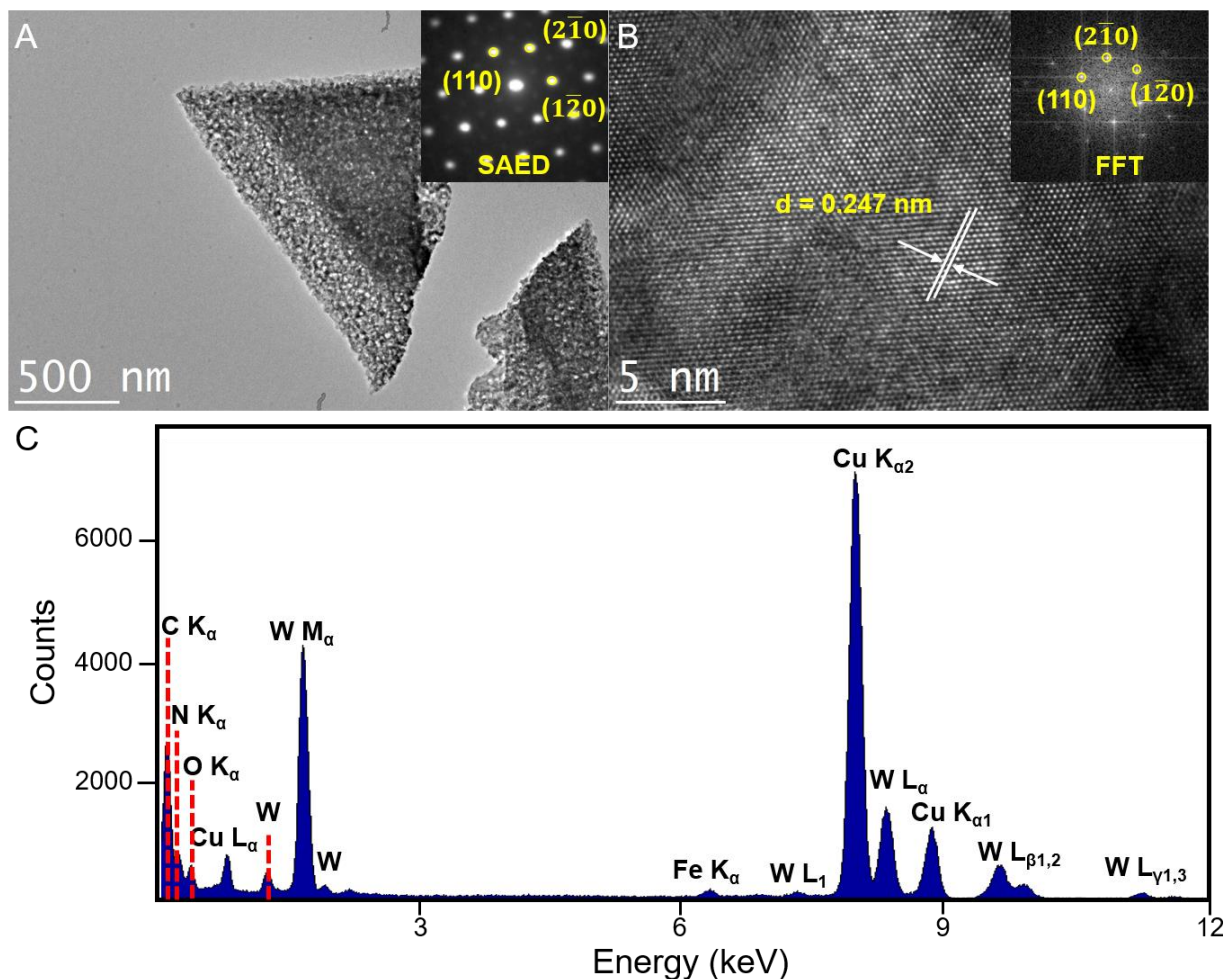


Fig. S14. TEM and EDS characterizations of W_5N_6 converted from WS_2 . (A) Low magnification TEM image of W_5N_6 . Inset: Selected area electron diffraction (SAED). (B) High resolution TEM image of W_5N_6 . Inset: FFT of the image. (C) EDS spectrum of W_5N_6 flake. Cu peaks are from TEM grid.

To determine the phase and crystal structure of the flake, we performed transmission electron microscope (TEM) measurement on an as-prepared sample after transferred onto a TEM grid. The low magnification TEM image in fig. S12A shows the flake on a TEM grid, the rough surface is probably caused by KOH etching during the transfer process. The strong selected-area electron diffraction (SAED) pattern (fig. S12A inset) indicates the high crystallinity of the crystal. The

hexagonal pattern is consistent with the crystal structure of the W_5N_6 (48). High-resolution TEM (HRTEM) image is shown in fig. S12B, where no obvious defect is found in the sample. Additionally, the distance of 0.247 nm between the highlighted lattice planes is consistent with the d-spacing of (110) planes in W_5N_6 crystal, which is labeled in the fast Fourier transformation (FFT) pattern in the inset. Other two planes ($2\bar{1}0$) and ($1\bar{2}0$) are also labeled in the FFT pattern. EDS spectrum (fig. S12C) shows the presence of W and N elements and no peaks of S element is observed.